

X-Ray Measurement of Dark Matter “Temperature” in Abell 1795

Yasushi Ikebe,^{1,2} Hans Böhringer,³ and Tetsu Kitayama⁴

¹ *Joint Center for Astrophysics, University of Maryland, Baltimore County, 1000 Hilltop Circle, Baltimore, MD 21250, USA*

² *Code 661, NASA/Goddard Space Flight Center, Greenbelt Rd., Greenbelt, MD 20771, USA*

³ *Max-Planck-Institut für extraterrestrische Physik, Postfach 1312, 85741 Garching, Germany*

⁴ *Department of Physics, Toho University, Miyama, Funabashi, Chiba 274-8510, Japan*

We establish a method from an X-ray observation of a galaxy cluster to measure the radial profile of the dark matter velocity dispersion, σ_{DM} , and to compare the dark matter “temperature” defined as $\mu m_{\text{p}} \sigma_{\text{DM}}^2$ with the gas temperature. The method is applied to the XMM-Newton observation of Abell 1795. The ratio between the specific energy of the dark matter and that of the intra cluster medium (ICM), which can be defined as β_{DM} in analogy with β_{spec} , is found to be less than unity everywhere ranging ~ 0.3 – 0.8 . In other words, the ICM temperature is higher than the dark matter “temperature”, even in the central region where the radiative cooling time is short and cooling flow phenomena are expected to be observed. A β_{DM} value smaller than unity can most naturally be explained by heating of the ICM. The excess energy of ICM is estimated to be ~ 1 – 3 keV per particle. We show that either the kinetic energy of member galaxies or the mass accretion onto the central black hole are possible energy sources to prevent the ICM in the central region from cooling.

1. Introduction

Early X-ray imaging observations with the *Einstein* observatory and *ROSAT* showed that in the central regions of clusters of galaxies the radiative cooling time is shorter than the age of the universe (e.g., Canizares, Stewart, & Fabian 1983). As a result, the intra cluster medium (ICM) should cool down to form a cold ($T < 10^6\text{K}$) gas phase inducing a global inflow of gas. This “cooling flow” (see Fabian 1994 for a review) picture has been extensively discussed and formed a basic assumption in many arguments. The low resolution spectroscopy in 0.5–2 keV by *ROSAT* showed that in some clusters the ICM temperature actually decreases towards the center (e.g., Böhringer et al. 1994; David et al. 1994; Allen & Fabian 1994). Higher resolution spectroscopy in 0.5–10 keV with *ASCA*, however, can not be fully understood with the conventional cooling flow model. *ASCA* spectra of cooling flow clusters can be well explained by a two (hot and cool) phase plasma without significant excess absorption features (e.g., Ikebe et al. 1999; Makishima et al. 2001). A naive cooling flow model predicting a range of temperatures with intrinsic absorption could also fit the *ASCA* data but generally produce worse chi-square results (e.g., Allen et al. 2001). Most recently, very high resolution spectroscopy with XMM-Newton/RGS unambiguously showed that there is very little X-ray emission from gas cooler than certain lower cut-off temperatures of ~ 1 – 3 keV (Tamura et al. 2001; Kaastra et al. 2001; Peterson et al. 2001). Unless a large amount of cooled gas or the metals in the cold gas are hidden (Fabian et al. 2001a), there must exist a heating mechanism that prevents the ICM from radiative cooling.

The necessity of global heat input into the ICM in ad-

dition to gravitational heating has also been pointed out from the break of the self-similarity between dark matter and ICM, which is most clearly demonstrated in the X-ray luminosity–temperature relation (L – T relation). A simple scaling analysis (Kaiser 1986) suggests a relation of $L \propto T^2$, while observation shows $L \propto T^3$ (e.g., Edge & Stewart 1991; David et al. 1993; White et al. 1997; Wu et al. 1999). The break of the self-similarity is also seen in the entropy vs temperature relation. Ponman, Cannon, & Navarro (1999) showed that cooler systems ($T < 4$ keV) have entropies higher than achievable through gravitational collapse alone. Simulation studies show that the observed relations can be reproduced, if there is enough non-gravitational heat input into the ICM by feedback from galaxies (e.g., Metzler & Evrard 1994; Bower et al. 2001) or preheating before the cluster formation (e.g., Navarro et al. 1995; Tozzi & Norman 2000).

In order to shed some new light onto these “cooling flow phenomena” and “break of self similarity,” we, in the present paper, perform a comparison of the temperature distribution of the ICM to the distribution of the velocity dispersion of the dark matter. A parameter, $\beta_{\text{spec}} \equiv \sigma_{\text{gal}}^2 / (kT / \mu m_{\text{p}})$, is often used as a measure of the average kinetic energy per unit mass in galaxies relative to that in the ICM. From observations of many clusters, the mean β_{spec} is ~ 1 with large scatter (e.g., Wu et al. 1999), indicating that the energy equipartition between galaxies and ICM is roughly achieved on average. In analogy with β_{spec} , we can introduce $\beta_{\text{DM}} \equiv \sigma_{\text{DM}}^2 / (kT / \mu m_{\text{p}})$ for comparison between the mean kinetic energy of the dark matter and that of the ICM, and define the dark matter “temperature” as $kT_{\text{DM}} \equiv \mu m_{\text{p}} \sigma_{\text{DM}}^2$. Note that the above definition of “temperature”, by means of proton

mass instead of the actual mass of dark matter particles, is only for the sake of comparison with the gas temperature. Therefore we put “temperature” in quotes. We obtain, in this paper, the radial profile of the β_{DM} value observationally for the first time.

In Sect. 2, we describe the method of measuring the dark matter velocity dispersion in a cluster of galaxies from an X-ray observation. We applied the method to the XMM-Newton data of a prototypical cooling flow cluster, Abell 1795 (hereafter A1795), which is located at $z=0.0616$ (Struble & Rood 1987). The X-ray data analysis and results are presented in Sect. 3. Discussion and summary are found in Sect. 4 and Sect. 5, respectively. Throughout the paper, the Hubble constant is given as $70 h_{70} \text{ km s}^{-1} \text{ Mpc}^{-1}$, and a flat universe ($\Omega_{\text{m},0} = 0.3$, $\Omega_{\Lambda,0} = 0.7$) is assumed. At the redshift of A1795, $1''$ corresponds to 1.19 kpc.

2. Method of Measuring Dark Matter Velocity Dispersion

We use a simplified model cluster being composed of a hot plasma ICM with a temperature of 10^7 – 10^8 K, and dark matter made of collisionless particles. Under the assumptions of spherical symmetry and hydrostatic equilibrium, the ICM distribution is described by

$$\frac{GM}{R} = -\frac{k_{\text{B}}T_{\text{g}}}{\mu m_{\text{p}}} \left(\frac{d \ln n_{\text{g}}}{d \ln R} + \frac{d \ln T_{\text{g}}}{d \ln R} \right), \quad (1)$$

where $M(< R)$ is the total gravitating mass within a sphere of radius R , k_{B} is the Boltzmann constant, G is the Gravitational constant, $n_{\text{g}}(R)$ and $T_{\text{g}}(R)$ are the density and temperature of the ICM, respectively. From an X-ray observation, $n_{\text{g}}(R)$ and $T_{\text{g}}(R)$ are measured and $M(< R)$ can be obtained via eq. 1. When the dark matter particles tracing the same gravitational field are in steady state, they obey the Jeans equation

$$\frac{GM}{R} = -\sigma_{\text{DM}}^2 \left(\frac{d \ln \rho_{\text{DM}}}{d \ln R} + \frac{d \ln \sigma_{\text{DM}}^2}{d \ln R} \right), \quad (2)$$

where $\sigma_{\text{DM}}(R)$ is the one-dimensional radial velocity dispersion, and ρ_{DM} is the mass density, which is given as $\rho_{\text{DM}} = \frac{1}{4\pi R^2} \frac{dM}{dR} - \mu m_{\text{p}} n_{\text{g}}$. Therefore, once the total gravitating mass, M , and the gas density, n_{g} , profiles are obtained from an X-ray observation, eq. 2 contains only one unknown parameter, $\sigma_{\text{DM}}(R)$. Equation 2 can be rewritten in the form of an ordinary differential equation for σ_{DM}^2 as

$$\frac{d\sigma_{\text{DM}}^2}{dR} = -\frac{GM}{R^2} - \frac{\sigma_{\text{DM}}^2}{\rho_{\text{DM}}} \frac{d\rho_{\text{DM}}}{dR}, \quad (3)$$

which can be solved numerically under a given boundary condition to derive the velocity dispersion profile of the dark matter.

Although a steady state dark matter distribution is assumed above, a dark matter density profile should actually be growing as matter is falling onto the system from outside. A numerical simulation by Fukushima & Makino (2001) shows that the dark matter halo grows in a self-similar way, keeping the density profile in the central region unchanged. This justifies the assumption at least in the central region.

A similar technique as described above was used in determining the ICM temperature profile, using X-ray imaging data without spectroscopic information taken, e.g., with the *Einstein* observatory. A model profile for the total mass is assumed and the temperature profile is derived from the equation of hydrostatic equilibrium so that the observed brightness profile is explained (e.g., Fabian et al. 1981; Hughes 1989). Here we solve the Jeans equation instead in order to derive the dark matter velocity dispersion.

3. A1795 and the XMM-Newton Observation

An ideal opportunity to study the mass profile as well as the velocity dispersion profile of dark matter is provided by the XMM-Newton observation of a prototypical cooling flow cluster, A1795. Early X-ray imaging observations with the *Einstein* observatory and *ROSAT* showed that the X-ray emission from A1795 has almost circular symmetry with a small elongation along the north-south direction, which indicates that the cluster is well relaxed dynamically (Jones & Forman 1984; Buote & Tsai 1996). The radial brightness profile shows a huge central excess above a prediction from an isothermal β -model profile, and the central excess luminosity gives a mass deposition rate of $\sim 250 h_{70}^{-2} M_{\odot} \text{ yr}^{-1}$ based on the standard cooling flow interpretation (Edge et al. 1992; Briel & Henry 1996). From the 0.5–10 keV spectrum taken with ASCA, however, a significantly smaller mass deposition rate is obtained ($\sim 66 h_{70}^{-2} M_{\odot} \text{ yr}^{-1}$ Fabian et al. 1994; $\sim 70 h_{70}^{-2} M_{\odot} \text{ yr}^{-1}$ Xu et al. 1998; $\sim 150 h_{70}^{-2} M_{\odot} \text{ yr}^{-1}$ Allen et al. 2001). Instead of the cooling flow model, the ASCA spectrum can be best described with a two temperature model without excess absorption (Xu et al. 1998).

The XMM-Newton observation of A1795 was carried out during the performance-verification phase on June 26 2000 with total observing time of ~ 50 ksec. The ICM temperature profile obtained with EPIC MOS as well as EPIC PN were already reported by Tamura et al. (2001) and by Arnaud et al. (2001), showing that it is almost isothermal at ~ 6 keV in the 2–10' radius region, while it decreases towards the center reaching the minimum temperature at ~ 3 keV. The Chandra observation gives consistent results (Ettori et al. 2002). A high resolution spectrum from the central region obtained with XMM-Newton/RGS has been analyzed by Tamura et al. (2001), showing a lack of signature of cool gas components below ~ 3 keV and an upper limit of $77 h_{70}^{-2} M_{\odot} \text{ yr}^{-1}$ for the mass deposition rate is obtained if an isobaric cooling flow model is applied.

In this paper, we analyze the data taken with the XMM-Newton/EPIC PN to measure the total mass profile of A1795 and to derive the dark matter velocity dispersion profile using the method described in Sect. 2.

4. Analysis of the XMM-Newton Data and Results

4.1. Data Screening and Background Subtraction

A significant fraction of any XMM-Newton observation is often contaminated by the huge background count

TABLE 1. BEST-FIT PARAMETERS OF THE DOUBLE β MODEL

parameter	value ^{a)}	
$\Sigma_{0,1}$	$(1.97 \pm 0.005) \times 10^{-3}$	[c/s/arcsec ²]
$R_{c,1}$	26.3 ± 0.4	[arcsec]
β_1	0.5927 ± 0.0003	
$\Sigma_{0,2}$	$(2.767 \pm 0.006) \times 10^{-4}$	[c/s/arcsec ²]
$R_{c,2}$	111 ± 1	[arcsec]
β_2	0.6457 ± 0.0002	
χ^2/ν	95.6/100	

^aErrors are 90% ($\Delta\chi^2 = 2.7$) confidence.

rate by soft proton flares. In order to derive time intervals with stable background, we eliminated time periods where the 0.5–10 keV count rate deviates from the mean value during quiescent periods by $\geq 2\sigma$. The total usable exposure time thus left is 23 ksec. Single and double pixel events are used in the present analysis.

After subtracting the out-of-time events (Strüder et al. 2001), the remaining background components are the cosmic X-ray background and the high energy particle events, which we estimated from the Lockman Hole data (Revolution # 70) and the filter-wheel-closed data (Revolution # 59), and subtracted.

4.2. Radial Count Rate Profile

Defining the center as the X-ray peak position, we have produced a projected-radial count-rate profile in the 0.5–10 keV band, which is illustrated in Fig. 1. Each X-ray photon is corrected with the vignetting function of the X-ray telescope. For comparison with the other X-ray observations, we quantified the radial profile using the β -model profile given by

$$\Sigma = \Sigma_0 \left[1 + \left(\frac{R}{R_c} \right)^2 \right]^{-3\beta+0.5}, \quad (4)$$

where R_c is a core radius and β is a beta parameter. The β model has often been used to fit X-ray brightness profile and generally gives a good representation for non cooling flow clusters. Since the X-ray brightness profile of A1795 has long been known to show a central excess above a β -model profile, we employed here a double β -model profile that is the sum of two β -model profiles to fit the observed 0.5–10 keV count rate profile within 848". In the actual fitting, the model brightness profile is convolved with the point spread function of the X-ray telescope¹, whose half-power-radius is $\sim 9''$ at 1.5 keV on-axis and significantly effects several of the central bins. Evaluating the goodness of the fit with a chi-square

¹ The PSF is approximated by an analytic function given as $\left[1 + \left(\frac{r}{r_c} \right)^2 \right]^{-\alpha}$, where r_c and α depend on off-axis angle as well as X-ray energy (see Ghizzardi 2001). We assumed that the PSF is constant in the entire FOV and independent of the X-ray energy. Parameters employed are $r_c = 5.37''$ and $\alpha=1.5$ that represent on-axis PSF at 1.5 keV for EPIC-PN (as given in a CCF file, XTR3_XPSF_0003.CCF).

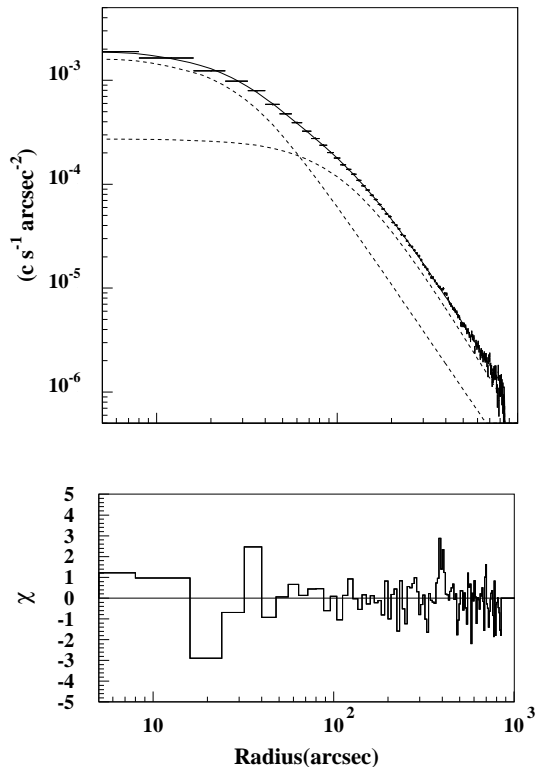


FIG. 1.— In the upper panel, the 0.5–10 keV X-ray count rate profile shown in crosses is fitted with a double β -model (solid line). The dotted lines show the individual β -model components. The fit residuals are shown in the lower panel.

statistic, we obtained a good fit as shown in Fig. 1 with the best-fit parameters as summarized in Table 1.

4.3. ICM Temperature and Metallicity Profile

The temperature and metallicity profiles given by Tamura et al. (2001) were derived from the conventional annular spectral analysis, accumulating spectra from concentric annular regions in the projected 2-dimensional space. We derive here the temperature and metallicity profiles instead in 3-dimensional form from deprojected spectra. We first accumulate 13 annular spectra from the vignetting corrected count rate profiles in individual energy channels. The outer radii are 16, 32, 48, 64, 96, 128, 192, 256, 384, 512, 640, 768, and 848". Assuming there is no cluster emission beyond 848" from the cluster center, we deprojected the annular spectra to spectra for 13 three-dimensional shell regions. Since no intrinsic absorption is found even from the central region (Tamura et al. 2001), the X-ray emission from the cluster is entirely optically thin and the deprojection process is straightforward.

In the analysis below we used only the inner 10 deprojected spectra within the 512" radius, which is significantly smaller than the maximum radius of 848" for the deprojection. The artificial cut-off of the X-ray emission outside the maximum radius does not affect the resulting deprojected spectra within 512". In addition, the

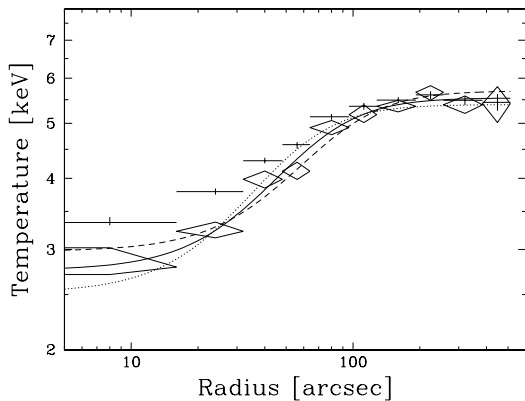


FIG. 2.— The temperature profile of A1795. Results from the deprojected spectra are shown with diamonds, while the conventional annular spectral analysis gives the profile with crosses. The solid line shows the best-fit function given as $T(R) = 5.54 - 2.79(1 + (R/65.0)^2)^{-1.5}$, while the dotted and dashed lines show extreme cases with the minimum and maximum for $R_{c,T}$ (see eq. 5), which are given as $T(R) = 5.39 - 2.88(1 + (R/51.4)^2)^{-1.5}$ and $T(R) = 5.70 - 2.72(1 + (R/82.8)^2)^{-1.5}$, respectively.

signal to noise ratios of the spectra within $512''$ are high enough, and some 10% systematic errors of the predicted background count rates introduce no significant systematic errors on temperature measurements.

We fitted each deprojected spectrum with a single-temperature plasma model. We employed the MEKAL model (Mewe et al. 1985, 1986; Kaastra 1992; Liedahl et al. 1995) and assumed the abundance ratio among different elements to have solar values. The fits are acceptable for all the ten spectra, and the deprojected temperature and metallicity profiles thus derived are illustrated in Fig. 2 and Fig. 3, respectively. Compared with the result from the conventional annular spectral analysis, the effect of the projection is clearly seen inside the $\sim 50''$ radius.

The temperature is consistent with being isothermal in the outskirts beyond 100 kpc, while towards the center it decreases monotonically and reaches 2.8 keV in the innermost shell. Note that the central minimum temperature agrees with the cut-off temperature in a cooling flow model that describes the RGS spectrum (Tamura et al. 2001) and the temperature of the X-ray filament detected with Chandra (Fabian et al. 2001). For usage in the following sections, we obtained an analytical formula that approximates the temperature profile. We fitted the temperature profile with a function given by

$$T(R) = T_0 - T_1 \left[1 + \left(\frac{R}{R_{c,T}} \right)^2 \right]^{-3/2}, \quad (5)$$

where T_0 , T_1 , and $R_{c,T}$ are free parameters to be determined by a χ^2 minimization. The parameters obtained are $T_0 = 5.54^{+0.25}_{-0.23}$, $T_1 = 2.79^{+0.35}_{-0.35}$, and $R_{c,T} = 65.0^{+13.6}_{-17.8}$, where the errors give the 90% confidence range for three parameters of interest ($\Delta\chi^2 = 6.25$). The best-fit function and extreme cases within errors are overlaid in Fig. 2, showing that the function gives a good repre-

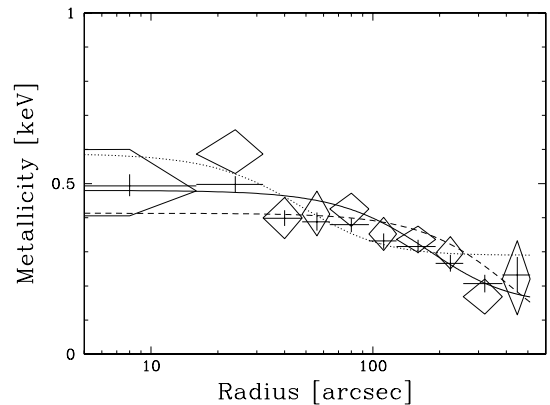


FIG. 3.— The metallicity profile of A1795. Results from the deprojected spectra are shown with diamonds, while the conventional annular spectral analysis gives the profile with crosses. The solid line shows the best-fit function given as $A(R) = 0.147 + 0.333(1 + (R/221)^2)^{-1.5}$, while the dotted and dashed lines show extreme cases with the minimum and maximum for $R_{c,A}$ (see eq. refeq:apro), which are given as $A(R) = 0.290 - 0.298(1 + (R/59.7)^2)^{-1.5}$ and $A(R) = 0 - 0.413(1 + (R/526.943)^2)^{-1.5}$, respectively.

sentation of the temperature profile.

In the metallicity profile (Fig. 3), the strong central concentration of metals found in the previous works (Tamura et al. 2001; Ettori et al. 2002) is confirmed. As for the temperature profile, the metallicity profile was also fitted with a similar function given as

$$A(R) = A_0 + A_1 \left[1 + \left(\frac{R}{R_{c,A}} \right)^2 \right]^{-3/2}. \quad (6)$$

We derived $A_0 = 0.15^{+0.16}_{-0.15}$, $A_1 = 0.33^{+0.20}_{-0.17}$, and $R_{c,A} = 221^{+306}_{-161}$, and the best-fit function and extreme cases within errors are overlaid in Fig. 3.

4.4. Mass Profile

An immediate way to derive the mass profile is using eq. 1 with the temperature profile measured in Sect. 4.3 and the density profiles of the ICM which can be obtained from the double β -model profile fitted to the observed X-ray brightness profile in Sect. 4.2. Assuming spherical symmetry, the projected count rate profile in the 0.5–10 keV band, $\Sigma(0.5\text{--}10\text{keV})$, gives the deprojected radial emissivity profile, $\epsilon(0.5\text{--}10\text{keV})$, which can be converted to the ICM density via the relation

$$\epsilon(0.5 - 10\text{keV}) = n_g^2 \Lambda(T, A; 0.5 - 10\text{keV}), \quad (7)$$

where $\Lambda(T, A; 0.5\text{--}10\text{keV})$ is the emissivity coefficient defined by temperature (T), metallicity (A), energy range (0.5–10 keV), and the instrument response.

The total gravitating mass profile thus derived with eq. 1 is shown in Fig. 4. Applying the different functions for the temperature profile that are the extreme cases within the measurement errors, we estimated typical errors for the total mass profile. The result roughly agrees with the mass profile given by Xu et al. (1998)

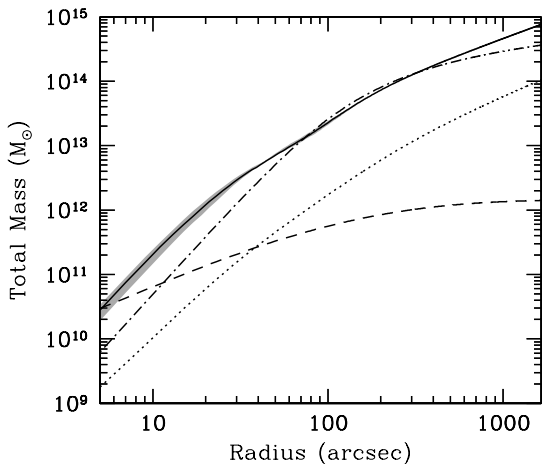


FIG. 4.— The integrated radial profile of the total gravitating mass is illustrated as the solid line with the gray error region. The solid line is obtained via eq. 1 from the best-fit brightness profile and the best-fit function for the temperature profile given in eq. 5. The lower and upper boundary of the error region correspond to the extreme cases for the temperature profile applied, where $R_{c,T}$ is the minimum and maximum value, respectively. The dotted line shows the ICM mass profile, which is calculated from integrating the density profile. The dashed line shows the stellar mass profile, which we calculate from an I -band image obtained by Johnstone et al. (1991), assuming a mass-to-light ratio of 0.8. The dot-dashed line indicates an approximated King profile (eq. 9 and 10) derived by fitting it to the data via eqs. 7 and 8.

derived from the ASCA data with the same method, although a shoulder-like structure found in their profile at ~ 100 kpc is less prominent in our profile. The difference in the mass profile is mainly attributed to different parameters of the double β -model profile fitted to the brightness profile.

4.5. Theoretical Modeling of the Mass Profile

The double β model applied to the X-ray brightness profile may be too restrictive to represent the underlying dark matter density profile. In the very central region, in particular, the double β model tends to require a flat core in the dark matter density profile, whereas a cuspy core is expected from a number of recent theoretical works (e.g., Navarro, Frenk, & White 1995; Fukushige & Makino 1997; Moore et al. 1999).

We therefore make an alternative approach from the derivation above. We start from modeling the total mass profile with a theoretically-motivated and representative model given by an analytical formula with a few free parameters. Being combined with the temperature profile derived in Sect. 4.3, the total mass profile is converted to the X-ray surface brightness profile of the cluster, which is fitted to the data to constrain the free parameters that specifies the mass profile. From eq. 1, a given total mass profile, $M(< R)$, and a temperature profile, $T(R)$, is converted to the ICM density profile as

$$n(R) = n_0 \frac{T(0)}{T(R)} \exp \left[- \int_0^R \frac{G\mu m_p M(< R)}{kT(R)R^2} dR \right], \quad (8)$$

where n_0 is the central ICM density. The emissivity profile in a given energy range, $\epsilon(E_1, E_2)$, is then obtained

by eq. 7, where n_g , T , A are substituted by eqs. 8, 5, and 6, respectively, which is then converted to the brightness profile, $\Sigma(E_1, E_2)$. Being convolved with the PSF, the model brightness profile is fitted to the 0.5–10 keV count rate profile observed to determine the best-fit parameters in the mass profile model.

As for the mass profile, we apply two representative models having a flat core and a cuspy core. The King model (King 1966) is a classic model for the gravitational potential structure characterized by a flat core. We used an approximated formula of the King model, in which the density profile is given as

$$\rho = \rho_0 \left[1 + \left(\frac{R}{R_c} \right)^2 \right]^{-3/2}, \quad (9)$$

while the integrated mass profile is given as

$$M(< R) = 4\pi R_c^3 \rho_0 \left[\ln \left(\frac{R}{R_c} + \sqrt{\frac{R^2}{R_c^2} + 1} \right) - \frac{R}{R_c} \left(\frac{R^2}{R_c^2} + 1 \right)^{-1/2} \right] \quad (10)$$

where ρ_0 is the central density and R_c is the core radius (see, e.g., Binney and Tremaine 1987). The predicted X-ray brightness profile from the King model is fitted to the 0.5–10 keV count rate profile. Fitting parameters are the core radius (R_c) and the central density (ρ_0) of the approximated King model, and the central ICM density (n_0). The best-fit model and the fit residuals are shown in Fig. 5 and the parameters are summarized in Table 2. The fit is not acceptable. In Fig. 4, the best-fit King model is compared with the mass profile obtained in Sect. 4.4, showing clearly that a central mass excess is necessary in addition to the King model mass.

We then added another King-model component to account for the central mass excess to construct a double approximated King model, which still has a flat core profile. Fitting parameters are now two sets with a core radius and a central density for each ($R_{c,1}$, $\rho_{0,1}$, $R_{c,2}$, and $\rho_{0,2}$), and the central ICM density (n_0). As shown in Fig. 5 and summarized in Table 2, a good fit was obtained.

Another analytical formula for the total mass profile we employed is the universal halo profile by Navarro et al. (1995, 1996, 1997; NFW model), which is characterized by a sharp central cusp. The density profile of the NFW model is given as

$$\rho = \rho_0 \left(\frac{R}{R_s} \right)^{-1} \left[1 + \left(\frac{R}{R_s} \right)^2 \right]^{-2}, \quad (11)$$

where R_s is called scale radius. The integrated mass profile of the NFW model is given as (Makino et al. 1998; Suto et al. 1998)

$$M(< R) = 4\pi \rho_0 R_s^3 \left[\ln \left(1 + \frac{R}{R_s} \right) - \frac{R}{R_s} \left(1 + \frac{R}{R_s} \right)^{-1} \right]. \quad (12)$$

The X-ray count rate profile predicted from the NFW model is fitted to the data, where the free parameters are ρ_0 , R_s , and n_0 . As illustrated in Fig. 5 and summarized

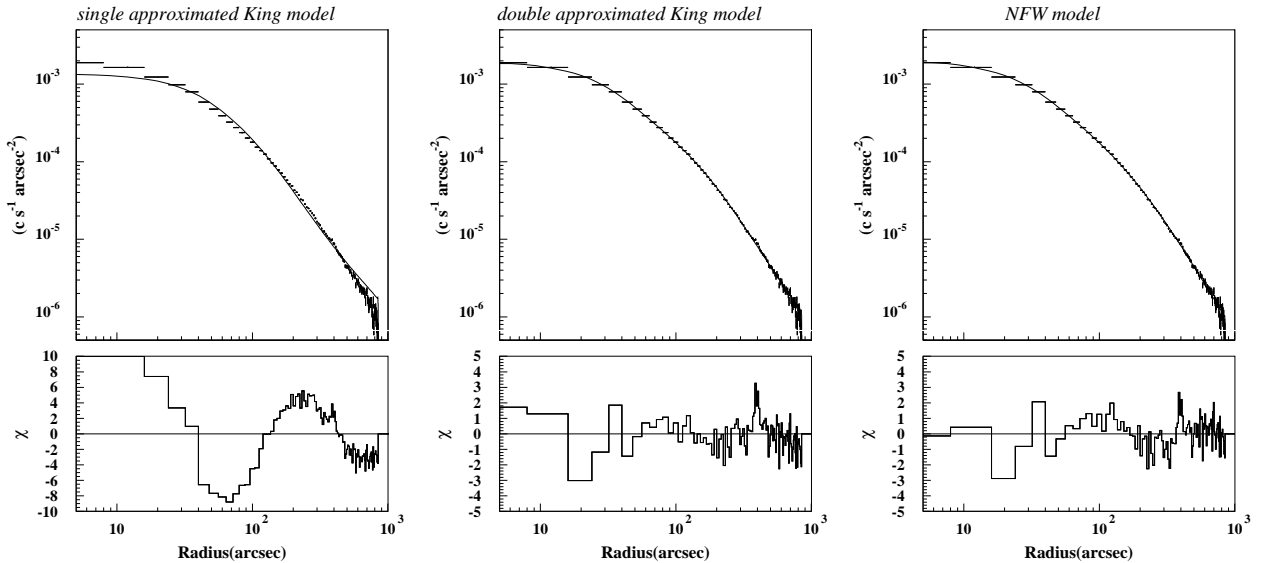


FIG. 5.— The upper panels show the 0.5–10 keV X-ray count rate profile (crosses) and the best-fit model profiles predicted from given total mass profiles. The mass profiles assumed in the model for the left, middle and right panel are a single approximated King model, double approximated King model, and NFW model, respectively. The lower panels show residuals for the best-fit model profiles.

TABLE 2. BEST-FIT PARAMETERS OF THE MASS PROFILE MODELS

mass model	$\rho_{0,1}$ ($M_{\odot}\text{arcsec}^{-3}$)	$R_{c,1}$ (arcsec)	$\rho_{0,2}$ ($M_{\odot}\text{arcsec}^{-3}$)	$R_{c,2}$ (arcsec)	$n_g(0)$ (cm^{-3})	χ^2/ν	R_{vir} (arcsec (Mpc))	M_{vir} (M_{\odot})
single King	1.18×10^7	99	0.075	1794/103
double King	4.47×10^7	27.6	3.30×10^6	180	0.116	123/101	1687 (2.0)	5.1×10^{14}
NFW	ρ_0 1.76×10^6	R_s 313	0.150	109/103	1913 (2.3)	7.5×10^{14}

in Table 2, the NFW model reproduces the data very well.

For each best-fit mass profiles, the double approximated King model and the NFW model, the corresponding virial mass, M_{vir} , and the virial radius, R_{vir} , are calculated and given in Table 2. The concentration parameters of the NFW model defined as $c \equiv R_s/R_{\text{vir}}$ is obtained to be 6.1. It is worth mentioning that the obtained c and M_{vir} are consistent with the theoretically predicted $c-M_{\text{vir}}$ relation (e.g., Bullock et al. 2001). The double approximated King model and the NFW model obtained above are compared in Fig. 6, together with the mass profile obtained in Sect. 4.4. The three mass profiles are all consistent within a 20–600'' radius region, and they approximately follow $M \propto R^{1.7}$ in the 30–200'' radius region. In Fig. 7, the double King model and the NFW model are compared in the mass density profile, together with the corresponding ICM density profile. As clearly seen in Fig. 6 and 7, the two theoretical model profiles differ most significantly in the very central region within $\sim 20''$ radius, where XMM can not well resolve the spatial structure. Ettori et al. (2002), using Chandra data, obtained the total mass profile in A1795 with finer spatial resolution and found that the density approximately follows $\rho \propto R^{-0.6}$ in the central region.

This profile is steeper than the King model ($\rho \propto R^0$) and flatter than the NFW model ($\rho \propto R^{-1}$) near the center. Therefore, the two mass profiles give a conservative mass range. In the next subsection, for determining the dark matter velocity dispersion profile, we use both the double approximated King model and the NFW model for the total mass profile model, which would also be expected to give conservative range of velocity dispersion representing systematic uncertainty involved in the usage of a specific mass profile model.

4.6. Dark Matter Velocity Dispersion Profile

We now calculate the dark matter velocity dispersion profile by solving the differential equation given in eq. 3. As the total mass profile, $M(<R)$, the double approximated King model or the NFW model profile obtained in Sect. 4.5 is employed, while the dark matter density profile is obtained from the total mass and the corresponding ICM density profile by $\rho_{\text{DM}}(R) = \frac{1}{4\pi R^2} \frac{dM(<R)}{dR} - \mu m_p n_g(R)$. Both $M(<R)$ and $\rho_{\text{DM}}(R)$ are substituted in eq. 3 and the differential equation is solved with the fourth-order Runge-Kutta method for various boundary conditions at the center, i.e. $\sigma_{\text{DM}}^2(0)$.

Figure 8 shows a set of solutions of eq. 3, when the best-fit NFW model is applied to $M(<R)$. Depending

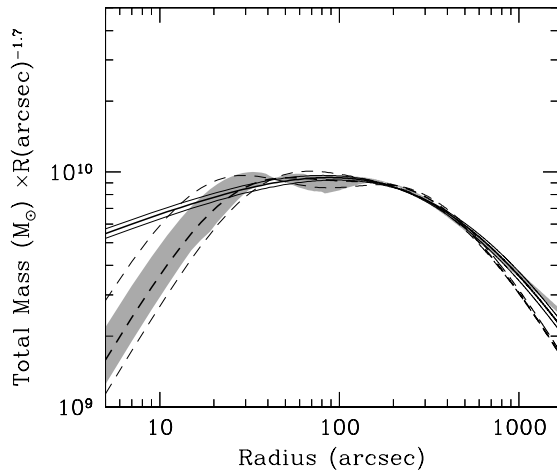


FIG. 6.— The scaled total mass profiles obtained in Sect. 4.4 (gray band) and the two theoretical models, the double approximated King model (dashed lines) and the NFW model (solid lines) obtained in Sect. 4.5 are compared. The vertical axis shows the integrated mass multiplied by $R^{-1.7}$. The bold lines represent solutions obtained from the best-fit function for the temperature profile given in eq. 5, while the thin lines correspond to the extreme cases obtained from the temperature profiles with the minimum and maximum value for $R_{c,T}$.

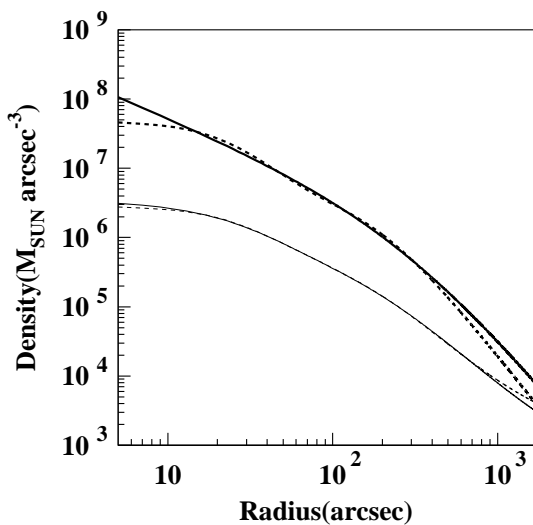


FIG. 7.— Mass density profiles of the total gravitating matter and the corresponding ICM density profiles that fit the observed 0.5–10 keV brightness profile are shown in the bold lines and in the thin lines, respectively. The solid lines show the result with the NFW model, while the dashed-lines show the result with the double approximated King model.

on the inner boundary condition, the dark matter velocity dispersion may fall to zero at small radii, or it may diverge to infinity. Among them, physically plausible solutions are selected so that the velocity dispersion at the virial radius is greater than 0 and less than the free fall velocity at the radius.

The velocity dispersion profiles thus obtained are shown in Fig. 9 individually for different mass models applied. In the central region, there is a clear difference between the results from the double approximated King model and the NFW model as expected

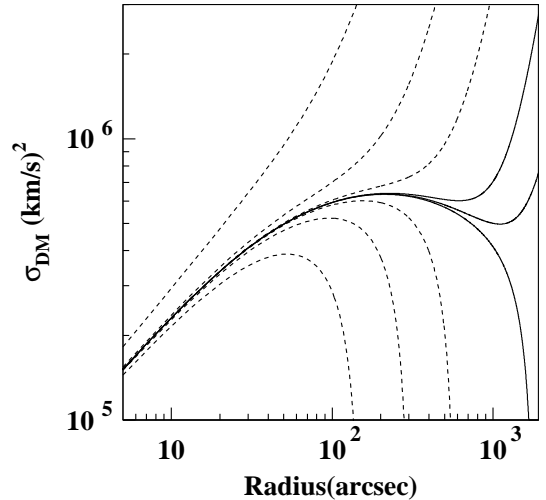


FIG. 8.— Solutions of eq. 3 with different $\sigma_{DM}(0)$ values, when the best-fit NFW model is used for the mass profile. Physically plausible solutions are illustrated in the solid lines, while the dashed lines are other possible solutions.

from their different behavior. The velocity dispersion is then converted to the “temperature” of the dark matter ($kT_{DM} \equiv \sigma_{DM}^2 \mu m_p$), which is compared with the ICM temperature in Fig. 10. The ICM temperature is greater than the dark matter “temperature” everywhere. Even in the central region where radiative cooling is expected to be most effective, the ICM temperature is significantly higher than that of the dark matter. The comparison of the temperatures can be more directly described by means of the β_{DM} value defined as $\beta_{DM} \equiv \sigma_{DM}^2 \mu m_p / kT = T_{DM} / T$, which ranges ~ 0.3 – 0.8 (Fig. 11). There is no sign that the ICM is cooled significantly below the dark matter “temperature”. In other words, the dark matter looks to form temperature floor that limits the ICM temperature.

As a matter of fact, what we derived by solving the Jeans equation is the velocity dispersion of the collisionless particles that includes the dark matter as well as the galaxies. However, as shown in Fig. 4, the galaxy component makes a minor contribution to the total mass and the derived velocity dispersion profile shown in Fig. 10 is virtually that of the dark matter, except in the very central region, where the galaxies amount to at most 40% within $\sim 10''$ radius. If the galaxies alone are in a steady state, they should also obey the Jeans equation under the same gravitational potential. The velocity dispersion profile of the member galaxies measured by den Hartog and Katgert (1996) is overlaid in Fig. 10, which shows a consistent profile with that of the dark matter in the case when the total mass profile is given by the NFW model.

5. Discussion

5.1. Robustness of the Results

As seen in Fig. 10, the ICM temperature profile and the dark matter “temperature” profile are found to have a similar shape. One concern regarding our result on the

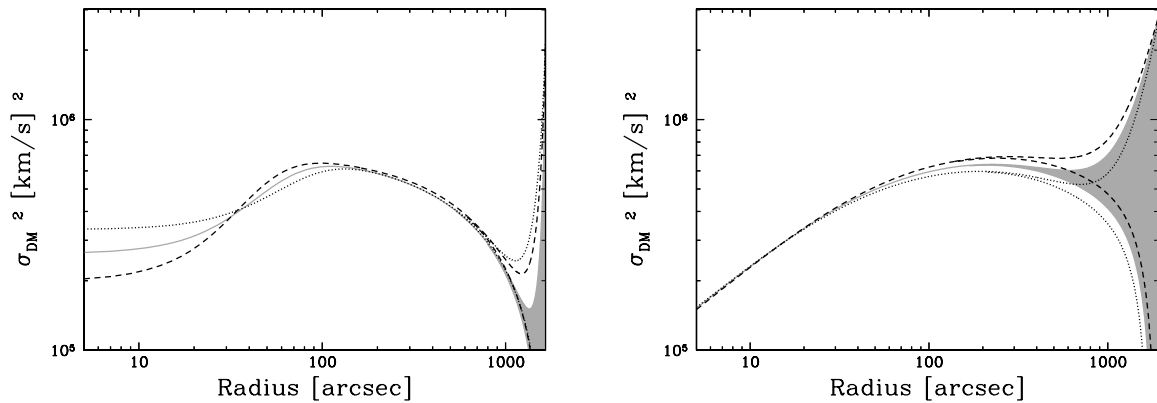


FIG. 9.— The velocity dispersion profile of the dark matter derived with the double approximated King model (left) or the NFW model (right) as the total mass profile. The gray hatched region shows the solutions that are obtained from the best-fit mass profile and satisfy the physically meaningful boundary condition. The dotted and dashed lines indicate the lower and upper boundary for solutions obtained from the extreme cases for the mass profile shown in Fig. 6.

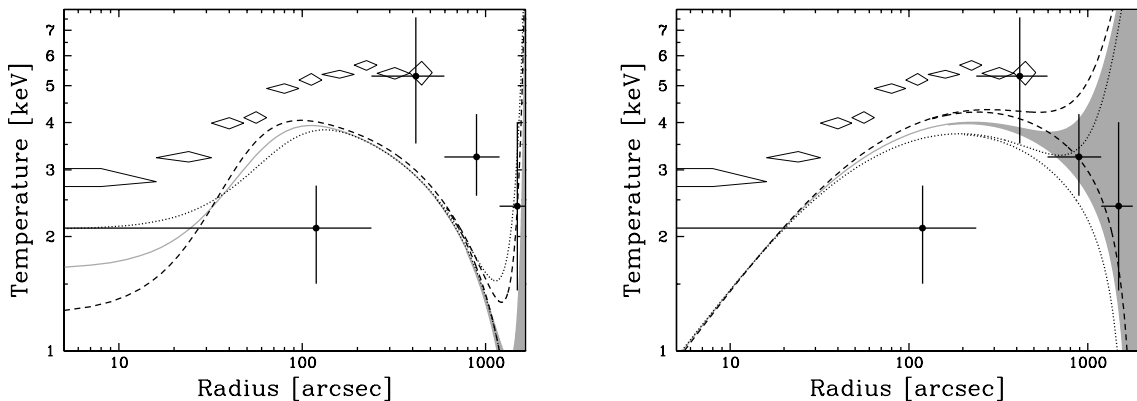


FIG. 10.— The velocity dispersion profiles shown in Fig. 9 are converted to “temperature” via $kT_{\text{DM}} = \mu m_{\text{p}} \sigma_{\text{DM}}^2$. The ICM temperature profile derived in Sect. 4.3 and shown in Fig. 2 is overlaid with diamonds. “Temperatures” of member galaxies derived by $\mu m_{\text{p}} \sigma_{\text{gal}}^2$ are also indicated with crosses, where the galaxy velocity dispersions (σ_{gal}) are taken from observations by den Hartog & Katgert (1996).

β_{DM} value is the fact that in order to measure the dark matter velocity dispersion the ICM temperature is used. I.e. the dark matter “temperature” and the ICM temperature are not entirely independently observed quantities. This might bring an essential problem to evaluate a derived parameter as the ratio β_{DM} .

Therefore we performed the following test. Using the observed count rate profile, we searched for the relation between an input ICM temperature and the resulting dark matter “temperature” that satisfies eq. 2. We repeat the analysis in Sect. 4.5 assuming a different ICM temperature profile from the one actually observed. Two cases are investigated. One is an isothermal ICM at 6 keV, and the other is a case where the ICM temperature decreases towards the center more dramatically than the actual profile as illustrated in Fig. 12. By fitting the count rate profile, we derived the total mass profile given by a double- or single-approximated King model, that reproduces the data. The dark matter “temperature” profile corresponding to each mass profile is ob-

tained by solving eq. 3. We find that in these two cases the dark matter “temperature” profile is completely different from the input ICM temperature profile as clearly seen in Fig. 12. These examples indicate that radial profiles of the ICM temperature and the dark matter “temperature” can take different forms and the β_{DM} value is not required to be similar everywhere. Therefore Nature must be choosing a particular solution for some physical reason.

We also investigate the effect of an anisotropy of the dark matter velocity distribution. Equation 2 is based on the assumption of isotropic motion of dark matter particles. However, simulation studies (e.g., Eke, Navarro, and Frenk 1998; Colín, Klypin, & Kravtsov 2000) indicate that the radial velocity dispersion, σ_{r}^2 , should be rather larger than the tangential velocity dispersion, $\sigma_{\text{t}}^2 \equiv \frac{1}{2}(\sigma_{\theta}^2 + \sigma_{\phi}^2)$. The degree of anisotropy is often measured with

$$A \equiv 1 - \frac{\sigma_{\text{t}}^2}{\sigma_{\text{r}}^2}, \quad (13)$$

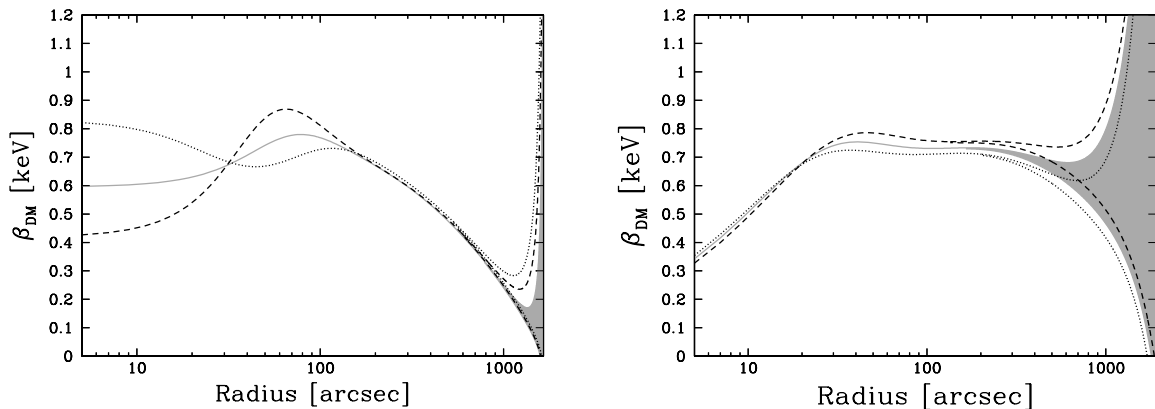


FIG. 11.— Radial profile of β_{DM} . The gray region, dotted lines, and dashed lines correspond to the different solutions in Fig. 9.

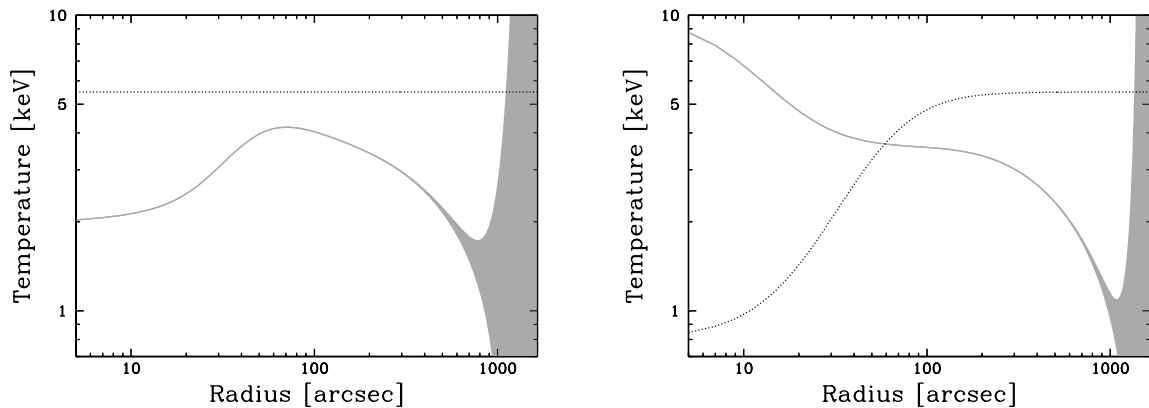


FIG. 12.— The gray hatched region shows the dark matter “temperature” profile as obtained in Sect. 4 but with a different ICM temperature profile assumed, which is illustrated with the dotted lines. For modeling the total mass profile, a double approximated King model and a single approximated King model are used in the left panel and the right panel, respectively.

and the Jeans equation is modified as

$$\frac{GM}{R} = -\sigma_{\text{DM}}^2 \left(\frac{d \ln \rho_{\text{DM}}}{d \ln R} + \frac{d \ln \sigma_{\text{DM}}^2}{d \ln R} + 2A \right). \quad (14)$$

Employing $A = 0.65 \frac{4R/R_{\text{vir}}}{(R/R_{\text{vir}})^2 + 4}$ derived by Colín, Klypin, & Kravtsov (2000), which is as large as 0.5 at the virial radius, R_{vir} , and converging to 0 at the center, we solved eq. 14 as done in Sect. 4.6. The σ_{DM} profile thus derived for the case of the best fit NFW mass profile is shown in Fig. 13, overlaid with the $A = 0$ solution given in Fig. 11. With the anisotropy, the velocity dispersion remains practically unchanged.

5.2. Heating Source

The β_{DM} profile determined here from observations should provide information on the thermal history of the ICM. From numerical simulation studies, $\beta_{\text{DM}} \sim 1-1.4$ is expected, if there is no cooling or additional heating (e.g., Metzler and Evrard 1994; Navarro et al. 1995; Bryan & Norman 1998). An obvious way to explain the β_{DM} value smaller than unity in A1795 is heating of the ICM.

As suggested from the break of the self-similarity between dark matter and ICM, there should have been non-

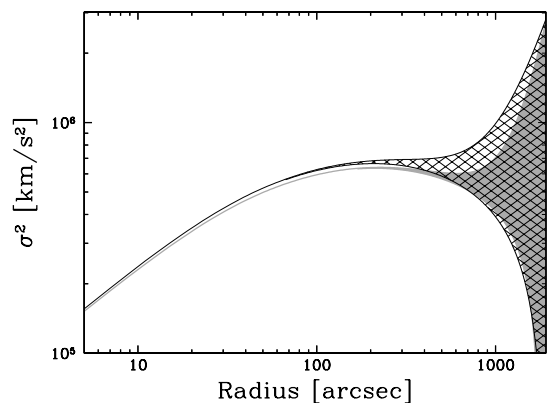


FIG. 13.— The hatched region with oblique lines shows the velocity dispersion profile of the dark matter, when the NFW model is used as the total mass profile and the anisotropy of the velocity distribution is introduced as $A = 0.65 \frac{4R/R_{\text{vir}}}{(R/R_{\text{vir}})^2 + 4}$. The solution in the isotropic case is overlaid with the gray hatched region.

gravitational heating acting globally. We, from our results, estimated the excess energy of the ICM over that

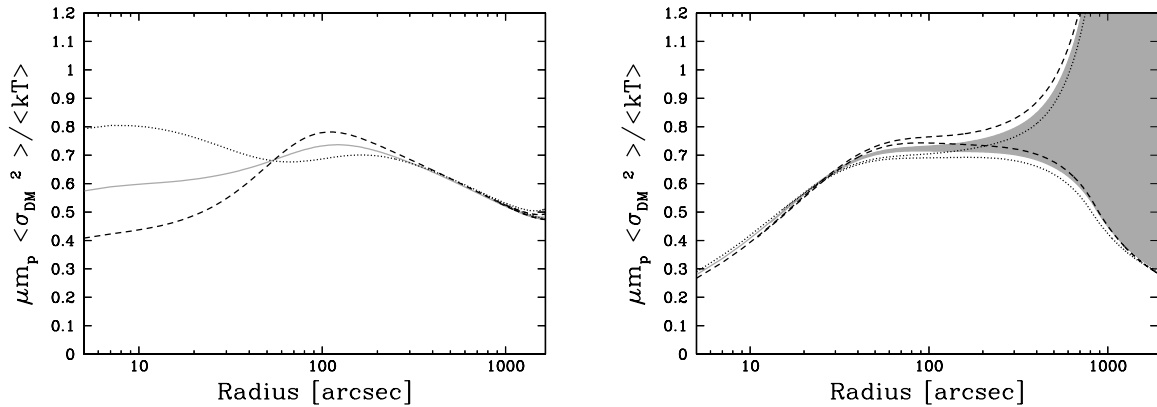


FIG. 14.— Radial profile of $\mu m_p \langle \sigma_{DM}^2 \rangle / \langle kT \rangle$. The gray region, dotted lines, and dashed lines correspond to the different solutions in Fig. 9.

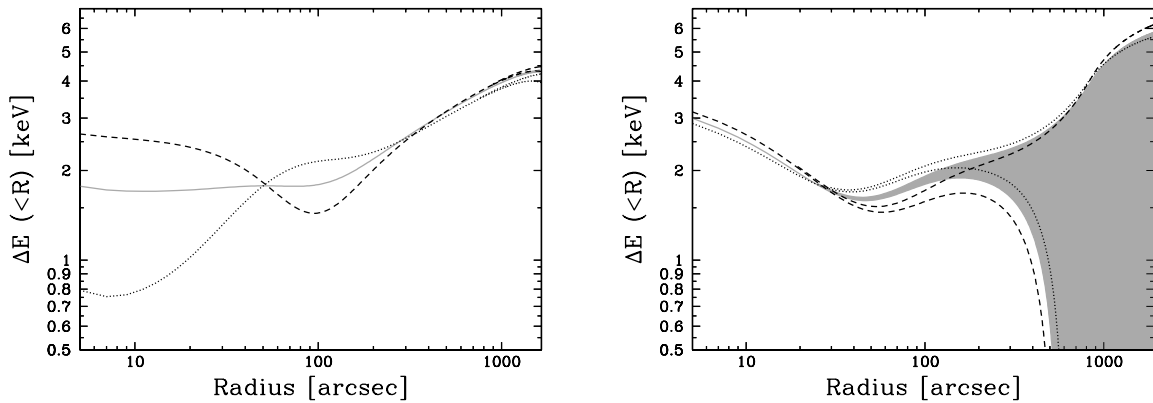


FIG. 15.— Radial profile of ΔE . The gray region, dotted lines, and dashed lines correspond to the different solutions in Fig. 9.

of the dark matter particles as

$$\begin{aligned} \Delta E(< R) &= \frac{3}{2} (\langle kT \rangle - \mu m_p \langle \sigma_{DM}^2 \rangle) \\ &= \frac{3}{2} \langle kT \rangle \left(1 - \frac{\mu m_p \langle \sigma_{DM}^2 \rangle}{\langle kT \rangle} \right), \end{aligned} \quad (15)$$

where $\langle \rangle$ denotes mass weighted mean within radius, R . Figures 14 and 15 show $\mu m_p \langle \sigma_{DM}^2 \rangle / \langle kT \rangle$ and ΔE thus derived, respectively. The excess energy of the ICM is found to be ~ 1 – 3 keV per particle, which may be compared with theoretical model predictions. The amount of energy injection to the gas phase that explains, e.g., the observed L – T relation depends on the period when the heating occurred. Heating prior to cluster collapse, “preheating”, needs 0.1–0.3 keV per particle (e.g., Navarro et al. 1995; Tozzi & Norman 2001), while heating after a cluster formation requires higher values of 1–3 keV per particle (e.g., Metzler & Evrard 1994; Loewenstein 2000; Wu, Fabian, & Nulsen 2000; Bower et al. 2001). Our results given above may indicate that the global non-gravitational heating that may cause the break of self-similarity has happened mainly within a collapsed cluster.

Even if such non-gravitational heating that explains the global X-ray feature of the cluster is provided, the central region of A1795 has a short radiative cooling time (Fig. 16) and a cooling flow is expected to be observed. According to a single-phase cooling flow model in a King-type potential well, the ICM temperature profile roughly follows $kT/\mu m_p \propto GM/R$ inside the core radius and reaches 0 at the center (Cowie and Binney 1977; Fabian, Nulsen, & Canizares 1984). On the other hand, the dark matter velocity dispersion is constant, and β_{DM} should increase towards the center. Such structure clearly contradicts the β_{DM} profile derived here. Therefore, there must be another significant energy input to the ICM in the central region at the present epoch to prevent the ICM from cooling.

As a possible energy source in the central region, we first consider gravitational energy of the member galaxies and stellar components therein. The kinetic energy of the random motion of stars can be partially transferred to the ICM by stellar mass loss. Gas supplied by stellar mass loss has velocities of the bulk motions of stars relative to the ICM, which is the sum of a galaxy motion and the motions of the stars in the galaxy, and is likely to

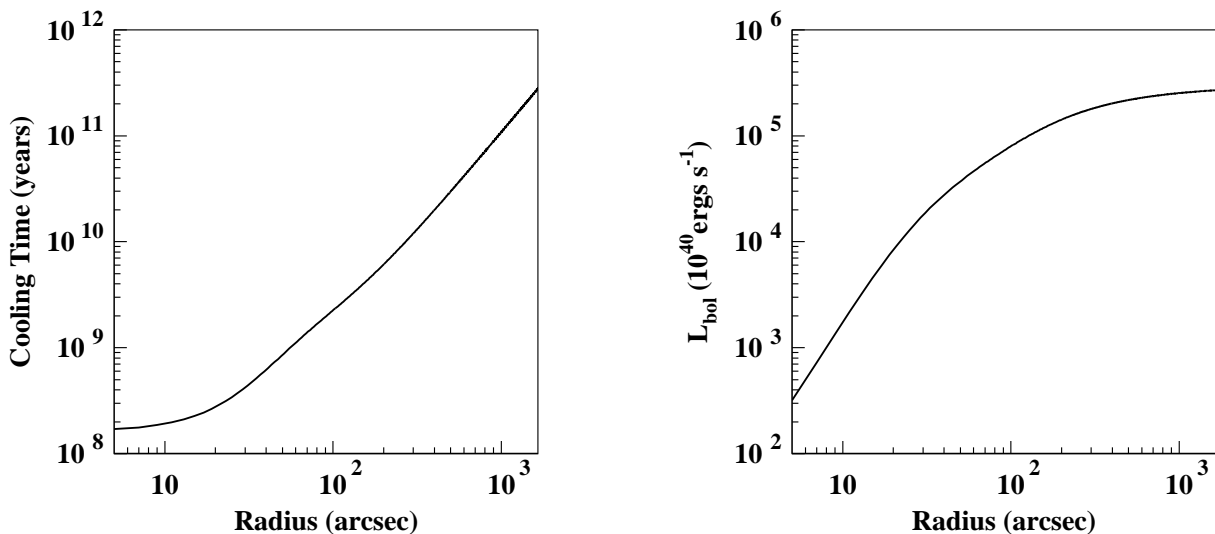


FIG. 16.— (Left panel) Radiative cooling time of the ICM calculated from the density and temperature at each radius. (Right panel) Bolometric luminosity integrated within each radius.

be thermalized by interactions with the ambient gas. If the stellar component moving in the same gravitational potential has similar velocity dispersion profile as that of the dark matter (Fig. 10), the gas temperature achieved from this process is expected to be comparable to the velocity dispersion of the dark matter. This process nicely accounts for X-ray emission from isolated X-ray compact elliptical galaxies (Matsushita 2001). The input rate of the kinetic energy of the gas from stellar mass loss may be simply estimated as $\dot{E} = 1/2 M_{\text{star}} \dot{m} \sigma^2 = 10^{42}$ ergs/s, where M_{star} is the total stellar mass of $1 \times 10^{12} M_{\odot}$, $\dot{m} = 3 \times 10^{11} M_{\odot} \text{ yr}^{-1}$ ($10^{11} M_{\odot}$) $^{-1}$ is the stellar mass loss rate in unit time, and $\sigma (= 580 \pm 80 \text{ km/s})$ is the velocity dispersion of the galaxies from den Hartog & Katgert (1996; Fig. 10). (The stellar velocity dispersions in the galaxies are smaller and neglected here.) This is much smaller than the output energy in the central region by X-ray radiation in galaxy clusters like A1795, however. Thus for the case of galaxy clusters, we have to look for additional heat sources.

Kinetic energy of stellar component might be more efficiently transferred to ICM via magnetic fields. As pointed out by, e.g., Makishima et al. (2001), the motion of stars may amplify interstellar magnetic fields and reconnections of the fields may heat up the ICM rather efficiently. The galaxies must have lost their kinetic energies through interactions with the ICM and have gradually fallen inwards accumulating onto the central galaxy to form the cD galaxy. A deep optical image of the cD galaxy in A1795 derived by Johnstone et al. (1991) shows a concentration of elliptical galaxies of various sizes and stars forming a largely extended envelope with $131 h_{70}^{-1}$ kpc effective radius, which strongly suggests the on-going formation process of the cD galaxy. Quantitatively, the total amount of dynamical energy of the stellar component in the member galaxies that has

been lost in the past is estimated. The stellar component in the galaxies is assumed to have a negligibly small potential (U) and kinetic energy (K) before the formation of the cluster, and the current energy of the stars is estimated to be $U + K \sim -10^{62}$ ergs. If the energy has been released over the last 10 Gyr and has been spent in ICM heating, the heating luminosity is expected to be $\sim 3 \times 10^{44}$ ergs s^{-1} . This amounts to the bolometric luminosity of the ICM within $60 h_{70}^{-1}$ kpc (Fig. 16), and may be sufficient to sustain the thermal energy of the ICM against radiative cooling. This model predicts that the stellar velocity dispersion became smaller than that of ICM, i.e. $\beta_{\text{spec}} < 1$, which is consistent with the actual observed value in the central region (Fig. 10).

Alternatively, there may be sufficient non-gravitational heat input in the central region provided from an AGN in the cD galaxy. According to Churazov et al. (2001; 2002) and Böhringer et al. (2002), an outflow from an AGN forms hot bubbles of relativistic plasma, which are lifted up by buoyancy and dissipate their energy into the ambient gas. The heating mechanism is self regulated: the lower the entropy, the higher the accretion rate. A portion of the accretion power is dissipated back into the ICM to make its entropy high and regulate the accretion rate to achieve an equilibrium state. This process automatically prevents the persistence of cold and hence dense clouds. The cD galaxy of A1795 has a radio source, 4C26.42, and the existence of an AGN is evident. Using the physical state of the ICM in the center we can actually estimate the energy provided by the AGN by applying the Bondi accretion model. According to the well-known correlation of the black hole mass with the mass of the bulge component (Magorrian et al. 1998), the black hole mass is expected to be $\sim 6 \times 10^9 M_{\odot}$. Assuming that the gas profile is flat in the center, we can use the measured values of $n_g = 0.15 \text{ cm}^{-3}$ and $T_0 = 2.8 \text{ keV}$

to obtain the Bondi mass accretion rate

$$\dot{M} = 4\pi \cdot 0.25 \rho_{\infty} c_{s,\infty}^{-3} (GM_{\text{BH}})^2 \quad (16)$$

$$= 0.23 M_{\odot}/\text{yr} \left(\frac{n}{1 \text{cm}^{-3}} \right) \left(\frac{T}{1 \text{keV}} \right)^{-3/2} \times \left(\frac{M_{\text{BH}}}{6 \times 10^9 M_{\odot}} \right)^2, \quad (17)$$

where ρ_{∞} and $c_{s,\infty}$ are the density and sound velocity outside the Bondi accretion radius. We find $\dot{M} \sim 0.7 \times 10^{-2} M_{\odot}/\text{yr}$. Under the standard assumption of 10% of the accretion energy to be dissipated, the output energy is found to be $E = \dot{M} 0.1 c^2 \sim 4 \times 10^{43}$ ergs/s. This amounts the X-ray luminosity within only the ~ 20 kpc region. The Bondi accretion radius is estimated to be $R_B \sim GM_{\text{BH}}/c_s^2 \sim 30$ pc, much smaller than the resolution of the temperature and density structure that can be measured with XMM-Newton. If the ICM density is not uniform but is clumpy, the Bondi accretion rate should be significantly larger and the heating rate could also be larger than the above estimation. We can note that the ICM conditions might temporally vary and that we currently see a relatively low state.

6. Summary and Conclusions

We derived the dark matter velocity dispersion profile from an X-ray observation for the first time. Using the XMM-Newton EPIC/PN data of A1795, we derived β_{DM} of ~ 0.3 – 0.8 . Note again that the ICM temperature is larger than the dark matter “temperature” everywhere.

We also derived the excess energy in the ICM, ΔE , which is found to be ~ 1 – 3 keV per particle.

These results can be most naturally explained by the existence of a heat source. In addition to global non-gravitational heating of the ICM accounting for the break of the self similarity, sufficient energy input into the ICM in the central region is necessary to prevent the ICM from radiative cooling. We show that the kinetic energy of the stellar component would be a sufficient energy reservoir. Alternatively, self-regulated Bondi accretion of the active nucleus of the central cD may be providing significant heat input. Measuring β_{DM} and ΔE from sample clusters ranging from low to high masses would give a clue to revealing the heating mechanism.

We thank Kuniaki Masai for helpful discussions. We are also grateful to Paul Lynam for critically reading this manuscript. The paper is based on observations obtained with XMM-Newton, an ESA science mission with instruments and contributions directly funded by ESA Member States and the USA (NASA). The XMM-Newton project is supported by the Bundesministerium für Bildung und Forschung, Deutsches Zentrum für Luft und Raumfahrt (BMBF/DLR), the Max-Planck Society and the Haidenhain-Stiftung. We thank the XMM software team for providing the Software Analysis System (SAS) for the XMM-Newton data reduction. In particular, we express our gratitude to Michael Freyberg for helping the data analysis. We also acknowledge FTOOLS.

References

- Allen, S. W., Fabian, A. C., Johnstone, R. M., Arnaud, K. A. & Nulsen, P. E. J. 2001, MNRAS, 322, 589
- Allen, S. W. & Fabian, A. C. 1994, MNRAS, 269, 409
- Arnaud, M., Neumann, D. M., Aghanim, N., Gastaud, R., Majerowicz, S., & Hughes, J. P. 2001, A&A, 365, L80
- Binney, J., & Tremaine, S. 1987, GALACTIC DYNAMICS, Princeton University Press
- Böhringer, H., Briel, U. G., Schwarz, R. A., Voges, W., Hartner, G. & Trumper, J. 1994, Nature, 368, 828
- Böhringer, H., Matsushita, K., Churazov, E., Ikebe, Y., & Chen, Y. 2002, A&A, 382, 804
- Buote, D. A., & Tsai, J. C. 1996, ApJ, 458, 27
- Bower, R. G., Benson, A. J., Lacey, C. G., Baugh, C. M., Cole, S., & Frenk, C. S. 2001, MNRAS, 325, 497
- Bullock, J. S., Kolatt, T. S., Sigad, Y., Somerville, R. S., Kravtsov, A. V., Klypin, A. A., Primack, J. R., & Dekel, A. 2001, MNRAS, 321, 559
- Burkert, A. 1995, ApJ, 447, L25
- Briel, U. G., & Henry, J. P. 1996, ApJ, 472, 131
- Bryan, G. L. & Norman, M. L. 1998, ApJ, 495, 80
- Canizares, C. R., Stewart, G. C., & Fabian, A. C. 1983, ApJ, 272, 449
- Churazov, E., Brügggen, M., Kaiser, C. R., Böhringer, H., & Forman, W. 2001, ApJ, 554, 261
- Churazov, E., Sunyaev, R., Forman, W., Böhringer, H. 2002, MNRAS, 332, 729
- Colín, P., Klypin, A. A., Kravtsov, A. V. 2000, ApJ, 539, 561
- Cowie, L. L., & Binney, J. 1977, ApJ, 215, 723
- David, L. P., Slyz, A., Jones, C., Forman, W., Vrtilik, S. D., & Arnaud, K. A. 1993, ApJ, 412, 479
- David, L. P., Jones, C., Forman, W. & Daines, S. 1994, ApJ, 428, 544
- den Hartog, R., & Katgert, P. 1996, MNRAS, 279, 349
- Edge, A. C., & Stewart, G. C. 1991, MNRAS, 252, 414
- Edge, A. C., Stewart, G. C., & Fabian, A. C. 1992, MNRAS, 258, 177
- Eke, Navarro, & Frenk (1998), ApJ, 503, 569
- Ettori, S., Fabian, A. C., Allen, S. W., & Johnstone, R. M. 2002, MNRAS, 331, 635
- Fabian, A. C., Hu, E. M., Cowie, L. L., & Grindlay, J. 1981, ApJ, 248, 47
- Fabian, A. C., Nulsen, P. E. J., & Canizares, C. R. 1984, Nature, 310, 733
- Fabian, A. C. 1994, ARA&A, 32, 277
- Fabian, A. C., Arnaud, K. A., Bautz, M. W., & Tawara, Y. 1994, ApJ, 436, L63
- Fabian, A. C., Mushotzky, R. F., Nulsen, P. E. J., & Peterson, J. R. 2001a, MNRAS, 321, L20
- Fabian, A. C., Sanders, J. S., Ettori, S., Taylor, G. B., Allen, S. W., Crawford, C. S., Iwasawa, K., & Johnstone, R. M. 2001b, MNRAS, 321, L33
- Fukushige, T., & Makino, J. 1997, ApJ, 477, L9
- Fukushige, T., & Makino, J. 2001, ApJ, 557, 533
- Hughes, J. P. 1989, ApJ, 337, 21
- Ikebe, Y., Makishima, K., Fukazawa, Y., Tamura, T., Xu, H., Ohashi, T., & Matsushita, K. 1999, ApJ, 525, 58
- Johnstone, R. M., Naylor, T., & Fabian, A. C. 1991, MNRAS, 248, 18p
- Jones, C., & Forman, W. 1984, ApJ, 276, 38
- Kaastra, J.S. 1992, An X-Ray Spectral Code for Optically Thin Plasmas (Internal SRON-Leiden Report, updated version 2.0)
- Kaastra, J. S., Ferrigno, C., Tamura, T., Paerels, F. B. S., Peterson, J. R., & Mittaz, J. P. D. 2001, A&A, 365, L99
- Kaiser, N. 1986, MNRAS, 222, 323
- King, I. R. 1966, AJ, 71, 276
- Liedahl, D. A., Osterheld, A. L. & Goldstein, W. H. 1995, ApJ, 438, L115
- Loewenstein, M. 2000, ApJ, 532, 12
- Magorrian, J., Tremaine, S., Richstone, D., Bender, R., Bower, G., Dressler, A., Faber, S. M., Gebhardt, K., Green, R., Grillmair, C., Kormendy, J., & Lauer, T. 1998, AJ, 115, 2285
- Makino, N., Sasaki, S., & Suto, Y. 1998, ApJ, 497, 555

- Makishima, K. et al. 2001, PASJ, 53, 401
Matsushita, K. ApJ, 547, 693
Metzler, C. A., & Evrard, A. E. 1994, ApJ, 437, 564
Mewe, R., Gronenschild, E. H. B. M., & van den Oord, G. H. J. 1985, A&AS, 62, 197
Mewe, R., Lemen, J. R., & van den Oord, G. H. J. 1986, A&AS, 65, 511
Moore, B., Quinn, T., Governato, F., Stadel, J., Lake, G. et al. 1999, MNRAS, 310, 1147
Navarro, J. F., Frenk, C. S., & White, S. D. W. 1995, MNRAS, 275, 720
Navarro, J. F., Frenk, C. S., & White, S. D. M. 1996, ApJ, 462, 563
Navarro, J. F., Frenk, C. S., & White, S. D. M. 1997, ApJ, 490, 493
Peterson, J. R. et al. 2001, A&A, 365, L104
Ponman, T. J., Cannon, D. B., & Navarro, J. F. 1999, Nature, 397, 135
Suto, Y., Sasaki, S., & Makino, N. 1998, ApJ, 509, 544
Struble, M. F., & Rood, H. J. 1987, ApJS, 63, 543
Strüder et al. 2001, A&A, 365, 18L
Tamura, T. et al. 2001, A&A, 365, L87
Tozzi, P., & Norman, C. 2001, ApJ, 546, 63
White, D. A., Jones, C., & Forman, W. 1997, MNRAS, 292, 419
Wu, K. K. S., Fabian, A. C., & Nulsen, P. E. J. 2001, MNRAS, 318, 889
Wu, X., Xue, Y., & Fang, L. 1999, ApJ, 524, 22
Xu, H., Makishima, K., Fukazawa, Y., Ikebe, Y., Kikuchi, K., Ohashi, T., & Tamura, T. 1998, ApJ, 500, 738